



Science Arts & Métiers (SAM)

is an open access repository that collects the work of Arts et Métiers Institute of Technology researchers and makes it freely available over the web where possible.

This is an author-deposited version published in: <https://sam.ensam.eu>
Handle ID: <http://hdl.handle.net/10985/25244>



This document is available under CC BY-NC-ND license

To cite this version :

Hugo ROIRAND, Alessandro PUGLIARA, Anis HOR, Nicolas SAINTIER, Jacques LACAZE, Benoît MALARD - New insights on the origin of grain refinement in 316L additively manufactured alloys - Scripta Materialia n°249, - 2024

Any correspondence concerning this service should be sent to the repository

Administrator : scienceouverte@ensam.eu





New insights on the origin of grain refinement in 316L additively manufactured alloys

Hugo Roirand^{a,b,c}, Alessandro Pugliara^a, Anis Hor^b, Nicolas Saintier^c, Jacques Lacaze^a, Benoit Malard^{a,*}

^a CIRIMAT, Université de Toulouse, INPT, CNRS, UPS, 4 Allée Emile Monso, 31030 Toulouse, France

^b ICA, Université de Toulouse, CNRS, ISAE-SUPAERO, 3 rue Caroline Aigle, 31400 Toulouse, France

^c I2M, Arts et métiers ParisTech, CNRS, Esplanade des arts et métiers, 33400 Talence, France

ARTICLE INFO

Keywords:

Laser powder bed fusion
Grain refinement
316L stainless steel
Nano-oxides
Columnar to equiaxed transition

ABSTRACT

Based on new experimental observations, a comprehensive analysis of factors influencing microstructure refinement in laser powder bed fusion additive manufacturing of 316L stainless steel components is presented. In contrast to existing hypotheses, the study reveals that neither the solidification mode nor the mere presence of nano-oxides in powders suffices to fully elucidate the observed grain refinement. Instead, this research highlights the intricate interplay between a strongly ferrite forming composition and the simultaneous presence of Mn-Si nano-oxides as essential contributors to the microstructure refinement process. The study explores the role of heterogeneous nucleation mechanism involving nano-oxides and provides fresh insights into the solidification mechanisms in laser powder bed fusion process, enhancing our understanding of microstructure control in laser powder bed fusion processes and offering novel perspectives for advanced materials engineering.

Recent advancements in additive manufacturing (AM) processes unlocked novel possibilities for manufacturing industrial components including repair capabilities, intricate designs, and microstructure tailoring [1–3]. The mechanical properties of AM components are significantly influenced by both their chemical composition and multi-scale microstructure characteristics [4]. Thus, it is imperative to exert control over these parameters to govern and enhance the final properties of these components.

Under standard conditions, the laser powder bed fusion (LPBF) process is known to induce the development of elongated grains along the build direction, resulting in unwanted mechanical anisotropy, especially in the context of multi-axial loadings [5]. Consequently, there is a critical need to diminish grain size and replace elongated grains with fine equiaxed ones to mitigate mechanical anisotropy while enhancing strength.

Numerous ways are available for controlling the microstructure of LPBF components amongst which modification of LPBF parameters, such as laser power or velocity, is one clear option. Lower energy densities have been demonstrated to produce finer grains and a less anisotropic texture, although this alteration also influences defect distribution [5,6]. As a result, a trade-off must be found between

optimizing energy to minimize defects and limiting the energy range for microstructure modification.

An alternative approach involves modifying the laser scan strategy to alter local solidification conditions or to restrict grain elongation by employing pattern rotations between each layer [7]. However, controlling grain size remains challenging with this technique, and it also often modifies defect distribution, further limiting the range of microstructure control.

The most powerful technique for refining grain size and mitigating grain anisotropy inherited from the LPBF process involves modifying the used powder. The literature records instances of achieving very fine equiaxed grain structures in the LPBF process using specific powders [8–11]. The results presented herein confirm that powder selection can reduce grain size by an order of magnitude while promoting equiaxed grains, and demonstrate that this effect is consistently observed regardless of the energy parameters used.

However, the factors that explain grain refinement in 316L alloy powders have not yet been identified with any certainty. Various hypotheses exist, amongst which Ziri et al. [6] proposed that fine grains result from a ferrite → austenite solidification sequence influenced by the ferrite-forming element content. Alternatively, Chniouel [12]

* Corresponding author.

E-mail address: benoit.malard@ensiacet.fr (B. Malard).

<https://doi.org/10.1016/j.scriptamat.2024.116174>

Received 13 December 2023; Received in revised form 3 May 2024; Accepted 12 May 2024

Available online 17 May 2024

1359-6462/© 2024 The Authors. Published by Elsevier Ltd on behalf of Acta Materialia Inc. This is an open access article under the CC BY-NC-ND license (<http://creativecommons.org/licenses/by-nc-nd/4.0/>).

Table 1

Chemical composition of the 316L stainless steel powders (wt.%, balance Fe).

Element	Cr	Ni	Mo	Mn	Si	O	N	P	C	S
A	17.7	13.6	2.7	1.5	<0.1	0.04	0.01	<0.01	<0.01	0.002
B	17.7	11.9	2.3	1.5	0.2	0.04	0.01	<0.01	<0.01	0.004
ASTM A240	16.0–18.0	10.0–14.0	2.0–3.0	≤2.0	≤0.75	<0.1	≤0.1	≤0.045	≤0.03	≤0.030

Table 2

LPBF process parameters with the same scan strategy: Meander without rotation.

Name	V (mm/s)	P (W)	t (mm)	h (mm)	VED (J/mm ³)
Low Energy (LE)	700	275	0.05	0.12	65
High Energy (HE)	400	350	0.05	0.12	146

attributes fine equiaxed grains to the presence of nano-precipitates which act as heterogeneous nucleation sites during solidification. Monier et al. [8] propose a further nucleation mechanism, namely the presence of icosahedral short range order (ISRO) in the liquid that promotes nucleation of equiaxed grains as already evidenced for some face centred cubic alloys [13,14].

At present, none of these hypotheses is universally accepted and, more importantly, none is fully consistent with the observations presented below. This paper thus undertakes a comprehensive examination of these hypotheses in light of our new results and seeks to synthesize these perspectives to elucidate grain refinement in 316L LPBF alloy.

Two 316L stainless steel powders, designated as A and B and provided by Höganäs, were employed in this investigation. They have diameter in the range of 15–45 µm and their chemical compositions, as provided by Höganäs, are listed in Table 1 where they are compared to the ASTM A240 standard. The primary disparities in chemical composition relate to the Ni, Mo, and Si contents.

For each powder, specimens were fabricated using LPBF process (SLM 125HL machine) with two distinct sets of process parameters denoted as low energy (LE) and high energy (HE), as outlined in Table 2. The main differences between these two parameter sets lie in the laser power (P) and laser velocity (v), while the hatch distance (h) and layer thickness (t) remained constant. Consequently, the volumetric energy density (VED), defined by Eq. (1), varies from 65 J/mm³ for the LE set to 146 J/mm³ for the HE set.

$$VED = \frac{P}{Vht} \quad (1)$$

The specimens were examined in their as-built condition following standard metallographic preparation procedures outlined in a previous publication [7]. Electron back-scattered diffraction (EBSD) analyses were conducted using a JEOL 7100F scanning electron microscope (SEM) equipped with a Nordlys Nano CCD detector. Grain boundaries low limit was set at 10°. Micrographs were obtained after etching with *aqua regia* (HCl + HNO₃), and observations were carried out using a Zeiss Axiovert A1m optical microscope.

Fig. 1 presents the inverse pole figure (IPF), IPF maps and micrographs of specimens produced using powders A and B under LE and HE conditions. The IPF maps reveal a substantial reduction in grain size and a significant alteration in material texture for specimens fabricated with powder B compared to those obtained with powder A. IPF maps confirm the near-free texture of specimens obtained with B powder. Hence, it is evident that powder modification exerts a significant influence on the microstructure, whether under LE or HE parameter sets.

The examination of melt pools reveals no discernible alterations in morphology, size, or arrangement attributable to the alteration in powder composition. Consequently, the changes observed in Fig. 1 are primarily associated with solidification mechanisms stemming from the modification in powder composition. This implies that using powder composition for microstructural control is effective and can be

considered independently of energetic factors. As a result, parameter tuning can be pursued to minimize defects while optimizing powder composition to refine grain size.

After confirming the feasibility of substantial grain size reduction at both LE and HE levels, this study was devoted to elucidating the fundamental powder-related factors that exert influence on these microstructural modifications in LPBF parts. At first, both powder batches, A and B, were observed under a SEM, as illustrated in Fig. 2. As expected, the analysis revealed no discernible differences in either the size or morphology of the powders. Furthermore, both batches exhibited minimal satellite particles. Therefore, it is clear that neither the size distribution nor the morphology could explain the microstructure modification as seen in Fig. 1 and the explanation for this effect should lie in powder's composition.

Chemical composition is known to play a pivotal role in determining the sequence of phase solidification of stainless steels [15]. Specifically, alloys rich in ferrite-forming elements such as Cr, Si, Mo, Ti, Al, tend to initiate solidification with the formation of delta ferrite. On the contrary, high levels Ni, Cu, Mn, N or C favor austenite as a primary phase. In Fig. 3-a, alloys A and B are located in the (Ni,T) isopleth section calculated (with 17.7 wt.% Cr, 2.5 wt.% Mo and 1.5 wt.% Mn) using ThermoCalc code and the TCFE12 database. This suggests that alloy B likely solidifies initially as ferrite before transforming into austenite, while alloy A would probably solidify directly as austenite because of growth undercooling; see below.

The sensitivity to solidification rate was examined in light of previous works [15–17]. To this end, equivalent Cr content, Cr_{eq} , and equivalent Ni content, Ni_{eq} , were estimated through Eqs. (2) and (3) reported in Suutala's work [15] and commonly used in the literature [18–20]:

$$Cr_{eq} = \%Cr + 1.37\%Mo + 1.5\%Si + 2\%Nb + 3\%Ti \quad (2)$$

$$Ni_{eq} = \%Ni + 0.31\%Mn + 14.2\%N + 22\%C + \%Cu \quad (3)$$

Stainless steels can be discriminated as ferrite or austenite former depending on the ratio $\kappa = Cr_{eq}/Ni_{eq}$. However, an increase in solidification rate increases growth undercooling that favors primary austenite solidification for stainless steels whose composition is close enough to the peritectic valley as is the case of alloy A [16,17,21,22]. This suggested to plot the type of primary phase during solidification in a map of κ versus the solidification rate as in Fig. 3-b adapted from Miettinen [21] where it is seen that the primary austenite field extends at high growth rate. In LPBF process, the maximum solidification velocity corresponds to the scanning speed but the actual solidification rate can be considerably lower, and Yang et al. [23] calculated solidification rates in the range of 100–200 mm/s for a scanning speed of 750 mm/s. Therefore, alloys A and B have been positioned at a solidification velocity of 100 mm/s, corresponding to the upper limit of Miettinen's diagram (Fig. 3-b). Accordingly, alloy A is anticipated to exhibit primary austenite formation, while alloy B is expected to display primary ferrite formation during LPBF process.

It appeared of interest to look at the influence of the κ ratio on the final microstructure in the existing literature (Table 3). This comparison revealed that A powder exhibited a ratio similar to that used in many studies ($\kappa = 1.52$), whereas B powder displayed one of the highest ratios ($\kappa = 1.69$). Elongated grain microstructures, indicative of epitaxial solidification, have been obtained for a range of κ values from $\kappa = 1.41$ for Godec et al. [24], $\kappa = 1.52$ for alloy A in our study and up to $\kappa = 1.70$ for

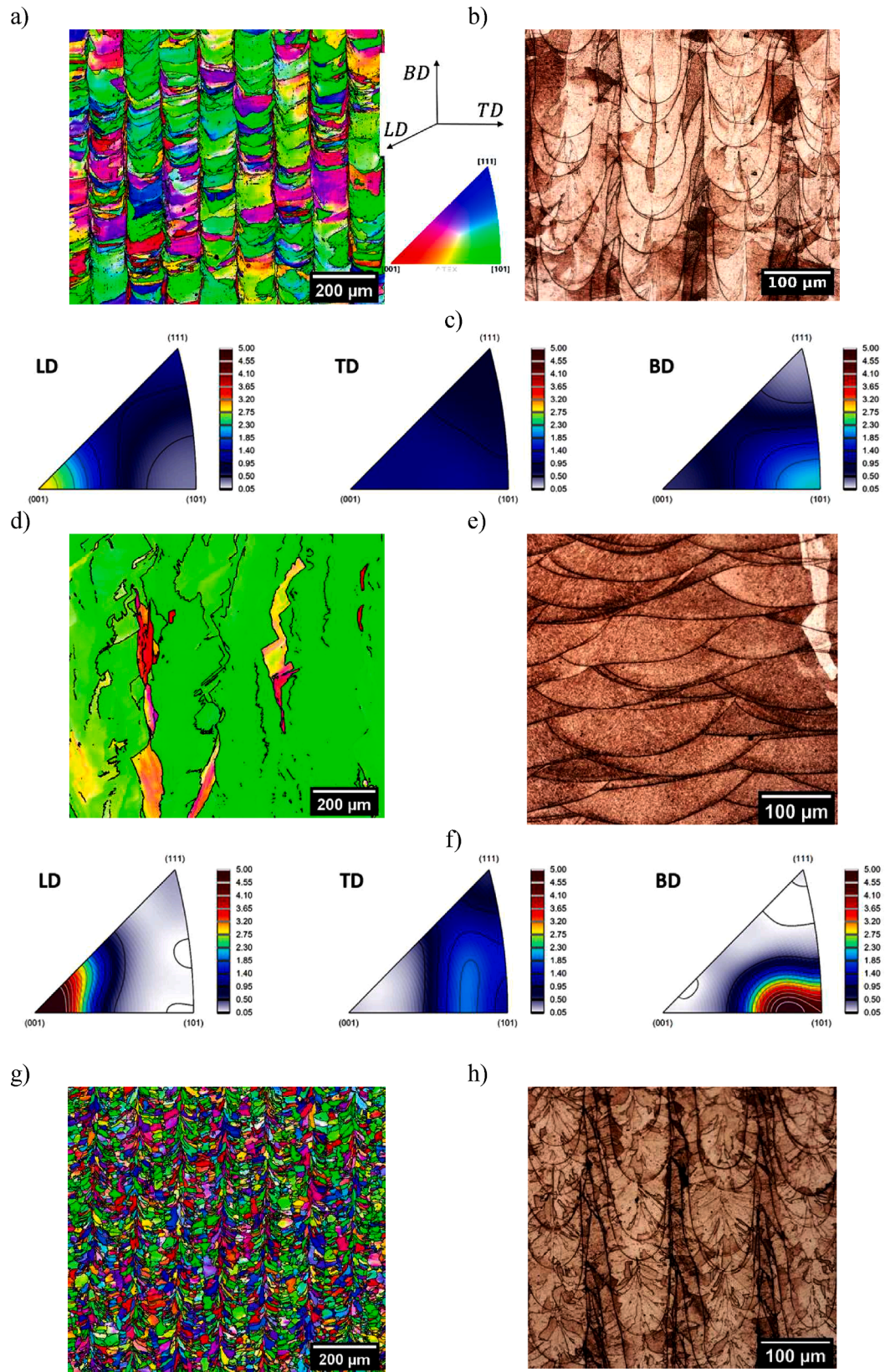


Fig. 1. Inverse pole figures, inverse pole figure map oriented along building direction (BD) and associated micrographs for specimens (a-c) A-LE, (d-f) A-HE, (g-i) B-LE and (j-l) B-HE. Texture index is multiple of random, mrd. LD is the laser direction and TD the transverse direction.

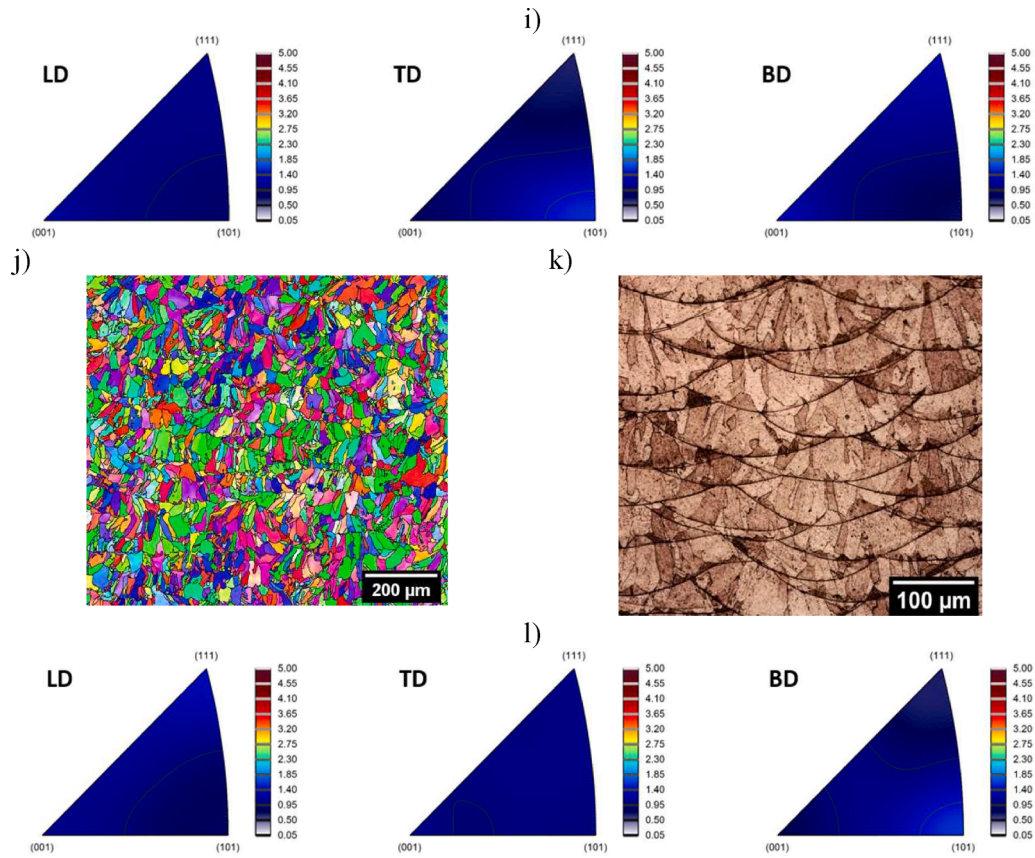


Fig. 1. (continued).

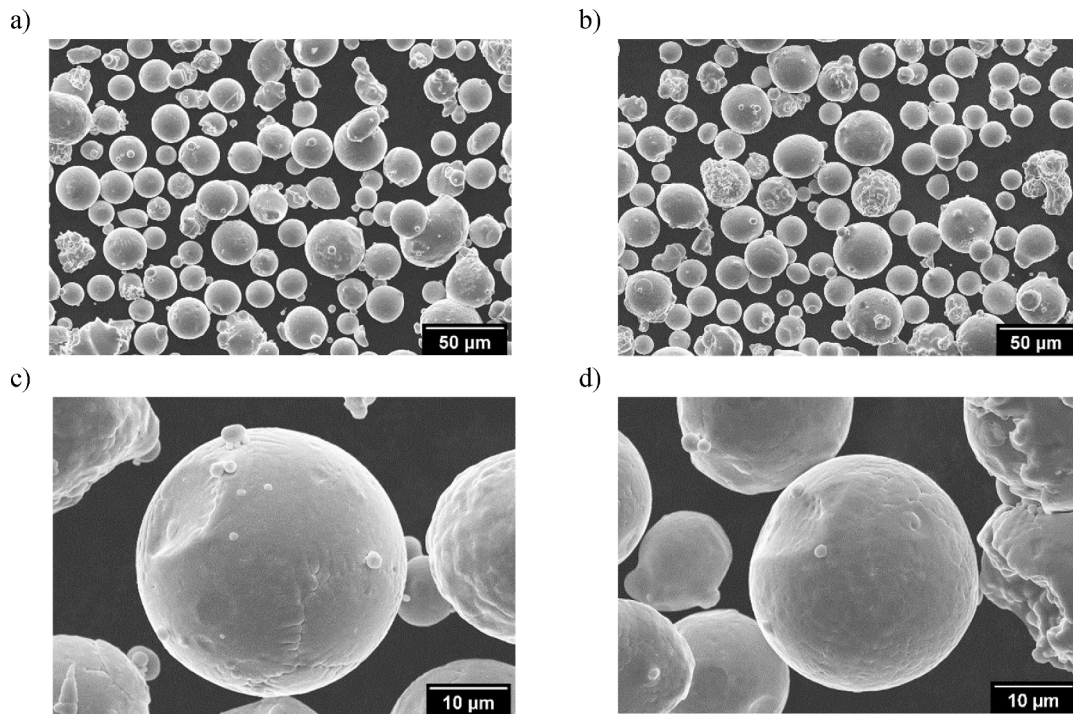


Fig. 2. SEM images from (a-c) A powder and (b-d) B powder.

Kurzynowski et al. [25]. However, fine grain microstructures have also been achieved with κ values in a range that overlaps the previous one, e. g. in studies by Chniouel ($\kappa = 1.63$) [12], Monier et al. ($\kappa = 1.66$) [8],

and Gray et al. ($\kappa = 1.77$) [26]. Thus, while the κ ratio alone does not fully explain the type of microstructure obtained in additive manufacturing, it can be stressed that fine/equiaxed grain

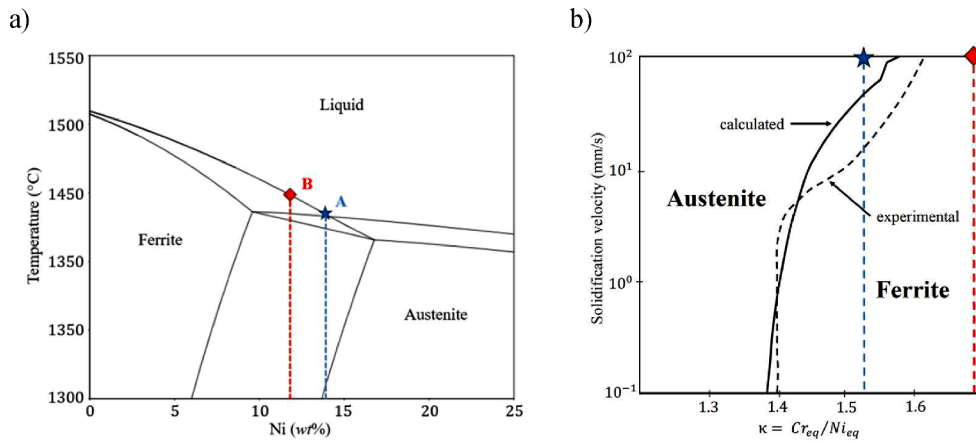


Fig. 3. (a) Isopleth Temperature-Ni section (calculated at 17.7 wt.% Cr, 2.5 wt.% Mo, 1.5 wt.% Mn) showing theoretical solidification sequences at equilibrium and (b) impact of solidification velocity on the primary phase formation (ferrite versus austenite) for 316 L, adapted from Miettinen [21].

Table 3

Comparison of Cr and Ni equivalent compositions and corresponding microstructures among additively manufactured 316L specimens reported in the literature. Microstructure type is defined as fine (F), columnar (C) or a mix of both (F/C).

Name	Cr_{eq} (%)	Ni_{eq} (%)	$\kappa = Cr_{eq}/Ni_{eq}$	Microstructure
A	21.5	14.2	1.52	C
B	21.2	12.5	1.69	F
Godec et al. [24]	21.9	15.5	1.41	C
Mower et al. [27]	20.9	14.3	1.46	C
Voisin et al. [28]	20.5	13.8	1.48	C
Andreau et al. [29]	21.8	14.6	1.49	C
Monier et al. (1) [8]	21.9	14.4	1.52	C
Chniouel (1) [12]	21.0	13.7	1.53	C
Zhai et al. [11]	21.3	13.4	1.59	C
Chniouel (2) [12]	21.3	13.1	1.63	F
Yang et al. [30]	20.2	12.2	1.66	C
Monier et al. (2) [8]	21.3	12.9	1.66	F
Byun et al. [31]	21.1	12.7	1.66	C/F
Dryepondt et al. [32]	21.1	12.6	1.68	C/F
Kurzynowski et al. [25]	21.2	12.5	1.69	C
Gray et al. [26]	24.0	13.5	1.77	F

microstructure has never been achieved for ratios smaller than $\kappa = 1.6$. In other words, while chemical composition alone does not entirely account for the observed microstructural refinement with B powder, it certainly plays a contributing role.

To explain why either elongated or fine grain microstructure could be achieved at $\kappa > 1.60$, the possibility of heterogeneous nucleation addressed in the introduction was considered. Possible nuclei could be either due to ISRO as suggested by Monier et al. [8] or to substrates present in the material. Monier et al. [8] observed grain refinement in an alloy containing 130 ppm of N but not with one containing 900 ppm, and thus suggested that ISRO could show up provided the N content is low enough. In the present case, both A and B powders had very low N content, less than 0.01 % as measured by Höganäs (Table 1) and respectively 84.3 ppm for A and 83.9 ppm for B as obtained by thermal desorption dosage with a Horiba EMGA-621 W machine. Based on Monier's finding [8], fine equiaxed microstructures should have been obtained also with powder B which is not the case as demonstrated with Fig. 1-a,c. Therefore, the ISRO-based solidification mechanism could be discarded and the focus shifted to finding an alternative heterogeneous nucleation mechanism by studying the original powders.

To achieve this, single powder grains from each batch were sectioned using focused ion beam (FIB) to extract foils for transmission electron microscopy (TEM) examinations that were carried out using a JEOL-2100F electron microscope operating at 200 kV. Electron images are illustrated in Fig. 4-a for powder A and Fig. 4-b for powder B. Further TEM observations of these foils (See Supplementary material section) revealed a similar microstructure between the two powder batches with grains of a few microns in size. The only major difference between the two powder batches was the evidence of particles with size up to 100 nm in powder B that appear in bright contrast in Fig. 4-b, while no such particles could be observed in powder A.

Higher magnification TEM micrographs, such as that shown in Fig. 4-c, revealed that the nano-precipitates have a core-shell structure with a well-defined interface with the matrix. In addition, numerical diffraction patterns obtained by fast fourier transform (FFT) of high-resolution TEM (HRTEM) images, like that in Fig. 4d, show that these nano-precipitates have an amorphous nature.

Additionally, their composition was analyzed in scanning transmission electron microscopy (STEM) mode using high-angle annular dark-field STEM (HAADF-STEM) images and an energy dispersive spectrometry (EDS) analyzer (Bruker SDD XFlash 5030) in TEM, indicating an enrichment in Mn, Si, and O compared to the matrix, along with a depletion in Fe, Cr, and Ni (Fig. 5). These precipitates are identified as mixed (Mn,Si) oxides or a combination of MnO and SiO₂ oxides.

These combined amorphous nano-oxides correspond to the observed amorphous core-shell structure (Fig. 4-c,d), with one oxide potentially forming the shell and the other the core. However, the EDS resolution was unable to confirm the composition of the internal phase. Nevertheless, nano-sized Mn-Si oxides are found in B powders, potentially serving as nucleation sites during solidification, thereby explaining the microstructural refinement. In fact, (Mn,Si) oxides have been systematically observed in as-built 316L components because of residual oxygen in the chamber [33] but this is their presence in the initial powder that appears instrumental for microstructure refinement. Indeed, inoculation through nanoscale precipitates is commonly used to reduce grain size and achieve less anisotropic microstructures in LPBF process on aluminum alloys [10,34], on Ti and NiTi alloys (see the review by Zhiyuan Liu et al. [35]), or else on ferritic steels [9]. However, it is worth mentioning that Chniouel [12] achieved columnar microstructures with a powder containing nano-oxides, demonstrating that the mere presence of nano-oxides does not fully account for the observed microstructural refinement. Because the alloy investigated by Chniouel had a low κ ratio at 1.53, it is most probable that a combined effect of nano-oxides present

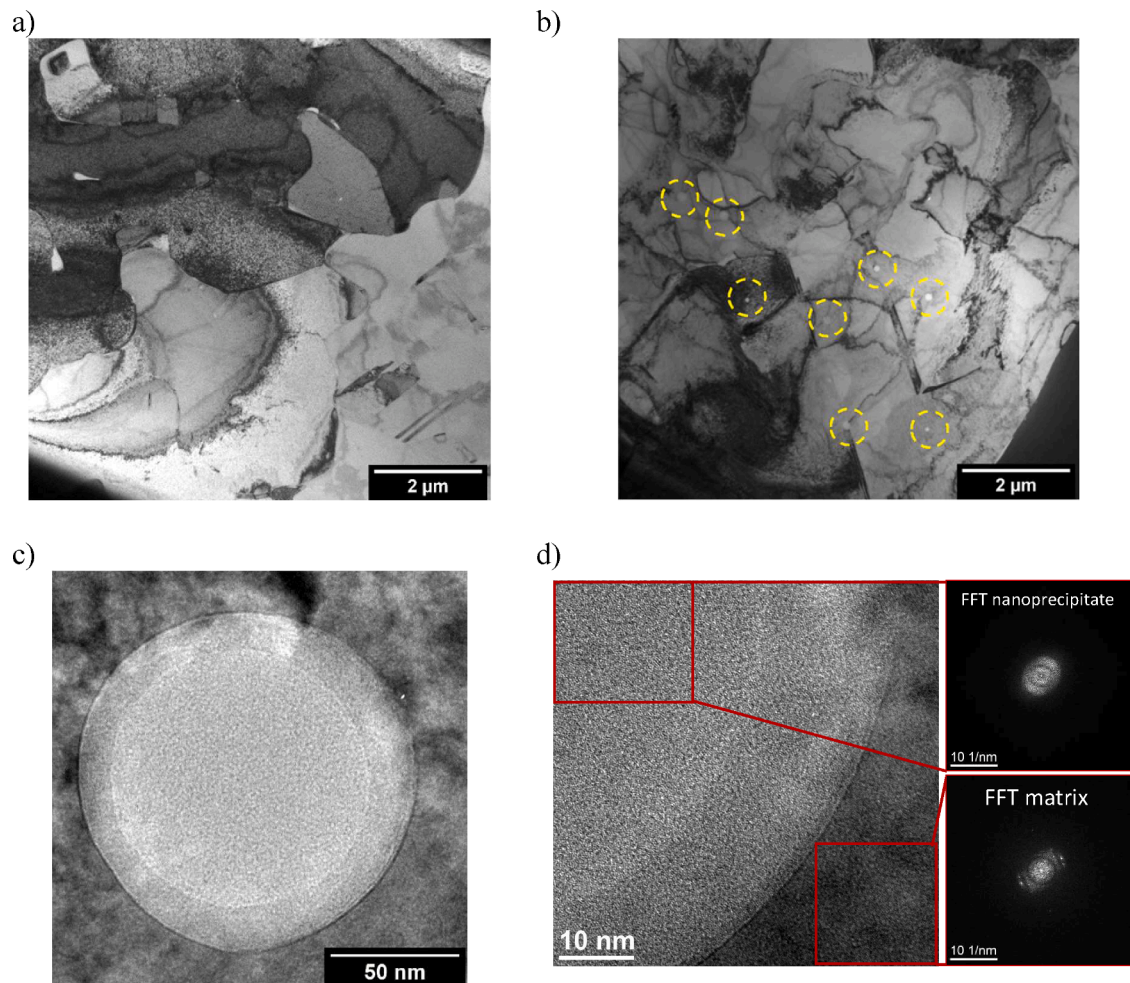


Fig. 4. Electron micrographs of a section from powder (a) A and (b) B. The yellow dashed circles in (b) locate the spherical nano-precipitates. (c) Electron micrograph and (d) HRTEM of a nano-precipitate identified in foil B with FFT of the central zone of an amorphous nano-precipitate and of the crystalline matrix near the nano-precipitate.

in the powder before LPBF processing and ferrite-forming composition contributes to equiaxed grain formation. Conversely, Godfrey et al. [36] studied an alloy at $\kappa = 1.67$ very close to our alloy B and did not notice any grain refinement but could evidence a competition between austenite and ferrite at the columnar solidification front.

In summary, it has been established through counter-examples that the κ ratio alone does not account for the powder's influence on grain refinement of 316L alloy, nor does it suffice to consider only the presence of nano-oxides. The most probable explanation is a process much alike the columnar to equiaxed transition in casting of metallic alloys and this is in this way that the effect of inoculation has been described [37]. During epitaxial solidification, the columnar front undergoes a growth undercooling that depends on both alloy composition and growth velocity. Heterogeneous substrates present ahead of this columnar front can grow with a lower growth rate and thus a lower growth undercooling than would the columnar front, and they will block it if they are numerous enough. These two conditions appear to be fulfilled in the case of alloy B thanks to its high κ value and to the presence of the Mn-rich nano-oxides.

CRediT authorship contribution statement

Hugo Roirand: Writing – original draft, Software, Methodology, Investigation, Formal analysis, Data curation, Conceptualization. **Alessandro Pugliara:** Investigation, Writing – review & editing. **Anis Hor:** Validation, Supervision, Project administration, Investigation, Funding acquisition. **Nicolas Saintier:** Validation, Supervision, Resources, Project administration, Funding acquisition. **Jacques Lacaze:** Writing – review & editing, Writing – original draft, Visualization, Validation, Software, Investigation, Formal analysis. **Benoit Malard:** Writing – review & editing, Writing – original draft, Validation, Supervision, Resources, Project administration, Investigation, Funding acquisition, Formal analysis, Conceptualization.

Declaration of competing interest

The authors declare that they have no known competing financial interests or personal relationships that could have appeared to influence the work reported in this paper.

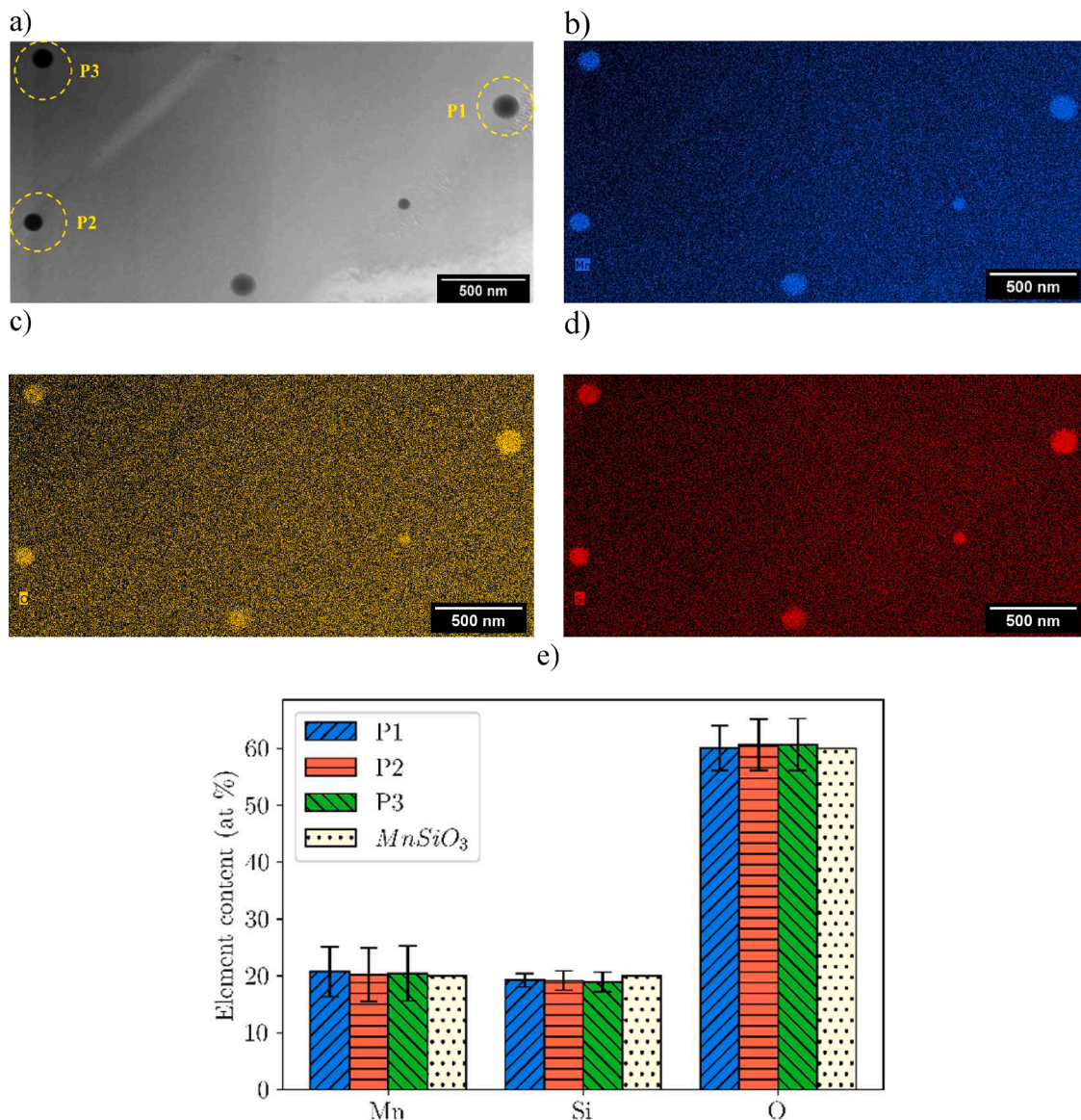


Fig. 5. (a) HAADF-STEM image and EDS maps of thin foil from B powder for (b) Mn signal, (c) O signal and (d) Si signal. (e) Elemental composition of three nano-precipitates determined by EDS and compared to $MnSiO_3$ theoretical composition.

Acknowledgments

The authors gratefully acknowledge Claudie Josse for preparing FIB samples at the Raymond Castaing Microcharacterization Center.

Funding

This work has been financially supported by the French National Center for Scientific Research (CNRS) as part of 80|PRIME program.

Supplementary materials

Supplementary material associated with this article can be found, in the online version, at [doi:10.1016/j.scriptamat.2024.116174](https://doi.org/10.1016/j.scriptamat.2024.116174).

References

- [1] Y. Balit, L.-R. Joly, F. Szymtka, S. Durbecq, E. Charkaluk, A. Constantinescu, Self-heating behavior during cyclic loadings of 316L stainless steel specimens manufactured or repaired by directed energy deposition, *Mater. Sci. Eng.* 786 (2020) 139476, <https://doi.org/10.1016/j.msea.2020.139476>.
- [2] B. Hanks, J. Berthel, M. Frecker, T.W. Simpson, Mechanical properties of additively manufactured metal lattice structures: data review and design interface, *Addit. Manuf.* 35 (2020) 101301, <https://doi.org/10.1016/j.addma.2020.101301>.
- [3] Z. Liu, et al., Additive manufacturing of metals: microstructure evolution and multistage control, *J. Mater. Sci. Technol.* 100 (2022) 224–236, <https://doi.org/10.1016/j.jmst.2021.06.011>.
- [4] T. DebRoy, et al., Additive manufacturing of metallic components – process, structure and properties, *Prog. Mater. Sci.* 92 (2018) 112–224, <https://doi.org/10.1016/j.pmatsci.2017.10.001>.
- [5] O. Gokcekaya, T. Ishimoto, S. Hibino, J. Yasutomi, T. Narushima, T. Nakano, Unique crystallographic texture formation in Inconel 718 by laser powder bed fusion and its effect on mechanical anisotropy, *Acta Mater.* 212 (2021) 116876, <https://doi.org/10.1016/j.actamat.2021.116876>.
- [6] S. Ziri, A. Hor, C. Mabru, Combined effect of powder properties and process parameters on the density of 316L stainless steel obtained by laser powder bed fusion, *Int. J. Adv. Manuf. Technol.* 120 (2022) 6187–6204, <https://doi.org/10.1007/s00170-022-09160-w>.
- [7] H. Roirand, A. Hor, B. Malard, N. Saintier, Effect of laser-scan strategy on microstructure and fatigue properties of 316L additively manufactured stainless steel, *Fatigue Fract. Eng. Mater. Struct.* 46 (2023) p32–p48, <https://doi.org/10.1111/ffe.13845>.
- [8] L. Monier, M. Buttard, M. Veron, J.J. Blandin, G. Martin, F. Vilaret, Y. Shen, B. Yrieix, C. Ernould, J. Guyon, A. Despres, On the origin of grain refinement and twin boundaries in as-fabricated austenitic stainless steels produced by laser powder bed fusion, *Addit. Manuf.* 61 (2023) 103351, <https://doi.org/10.1016/j.addma.2022.103351>.

- [9] A. Durga, N. Holländer Pettersson, S.B.A. Malladi, Z. Chen, S. Guo, L. Nyborg, G. Lindwall, Grain refinement in additively manufactured ferritic stainless steel by in situ inoculation using pre-alloyed powder, *Scr. Mater.* 194 (2021) 113690, <https://doi.org/10.1016/j.scriptamat.2020.113690>.
- [10] Q. Tan, Y. Yin, Z. Fan, J. Zhang, Y. Liu, M.-X. Zhang, Uncovering the roles of LaB₆-nanoparticle inoculant in the AlSi10Mg alloy fabricated via selective laser melting, *Mater. Sci. Eng. A* 800 (2021) 140365, <https://doi.org/10.1016/j.msea.2020.140365>.
- [11] W. Zhai, W. Zhou, S.M.L. Nai, Grain refinement of 316L stainless steel through in-situ alloying with Ti in additive manufacturing, *Mater. Sci. Eng.* 840 (2022) 142912, <https://doi.org/10.1016/j.msea.2022.142912>.
- [12] A. Chniouel, P.-F. Giroux, F. Lomello, P. Aubry, E. Vasquez, O. Hercher, H. Maskrot, Influence of substrate temperature on microstructural and mechanical properties of 316L stainless steel consolidated by laser powder bed fusion, *Int. J. Adv. Manuf. Technol.* 111 (11–12) (2020) 3489–3503, <https://doi.org/10.1007/s00170-020-06316-4>, déc.
- [13] J. Zollinger, M. Rappaz, Influence of minor additions on icosahedral short-range order (ISRO) and its consequences on nucleation and solidification growth kinetics in Fcc alloys, *IOP Conf. Ser.: Mater. Sci. Eng.* 529 (1) (2019) 012045, <https://doi.org/10.1088/1757-899X/529/1/012045>.
- [14] G. Kurtuldu, A. Sicco, M. Rappaz, Icosahedral quasicrystal-enhanced nucleation of the Fcc phase in liquid gold alloys, *Acta Mater.* 70 (2014) 240–248, <https://doi.org/10.1016/j.actamat.2014.02.037>.
- [15] N. Suutala, Effect of solidification conditions on the solidification mode in austenitic stainless steels, *Metal. Trans. A* 14 (1) (1983) 191–197, <https://doi.org/10.1007/BF02651615>.
- [16] S. Fukumoto, W. Kurz, Prediction of the delta to gamma. Transition in austenitic stainless steels during laser treatment, *ISIJ Int.* 38 (1) (1998) 71–77, <https://doi.org/10.2355/isijinternational.38.71>.
- [17] M. Bobadilla, J. Lacaze, G. Lesoult, Influence des conditions de solidifications sur le déroulement de la solidification des aciers inoxydables austénitiques, *J. Cryst. Growth* 89 (1988) 531–544, [https://doi.org/10.1016/0022-0248\(88\)90216-3](https://doi.org/10.1016/0022-0248(88)90216-3).
- [18] A. Di Schino, M.G. Mecozzi, M. Barteri, J.M. Kenny, Solidification mode and residual ferrite in low-Ni austenitic stainless steels, *J. Mater. Sci.* 35 (2000) 375–380, <https://doi.org/10.1023/A:1004774130483>.
- [19] M.A.V. Bermejo, T. Debroy, Tarasankar, K. Hurtig, L.E. Svensson, Towards a map of solidification cracking risk in laser welding of austenitic stainless steels, *Phys. Procedia* 78 (2015) 230–239, <https://doi.org/10.1016/j.phpro.2015.11.033>.
- [20] M. Pujar, R.-K. Dayal, T.P.S. Gill, S.N. Malhotra, Evaluation of microstructure and electrochemical corrosion behavior of austenitic 316 stainless steel weld metals with varying chemical compositions, *J. Mater. Eng. Perform.* 14 (3) (2015) 327–342, <https://doi.org/10.1361/10599490523977>.
- [21] J. Miettinen, Thermodynamic-kinetic simulation of constrained dendrite growth in steels, *Metal. Mater. Trans. B* 31 (2000) 365–379, <https://doi.org/10.1007/s11663-000-0055-6>.
- [22] J.-C. Lippold, Solidification behavior and cracking susceptibility of pulsed-laser welds in austenitic stainless steels, *Welding J. Including Welding Res. Suppl.* 73 (6) (1994) 129–139. ISSN 0043-2296.
- [23] D. Yang, Y. Yin, X. Kan, Y. Zhao, Z. Zhao, J. Sun, The mechanism of substructure formation and grain growth 316L stainless steel by selective laser melting, *Mater. Res. Express* 8 (9) (2021) 096510, <https://doi.org/10.1088/2053-1591/ac21ea>.
- [24] M. Godec, S. Zaefferer, B. Podgornik, M. Šinko, E. Tchernychova, Quantitative multiscale correlative microstructure analysis of additive manufacturing of stainless steel 316L processed by selective laser melting, *Mater. Charact.* 160 (2020) 110074, <https://doi.org/10.1016/j.matchar.2019.110074>.
- [25] T. Kurzynowski, K. Gruber, W. Stopyra, B. Kuźnicka, E. Chlebus, Correlation between process parameters, microstructure and properties of 316 L stainless steel processed by selective laser melting, *Mater. Sci. Eng.* 718 (2018) 64–73, <https://doi.org/10.1016/j.msea.2018.01.103>.
- [26] G.T. Gray, V. Livescu, P.A. Rigg, C.P. Trujillo, C.M. Cady, S.R. Chen, J.S. Carpenter, T.J. Lienert, S.J. Fensin, Structure/Property (constitutive and spallation response) of additively manufactured 316L stainless steel, *Acta Mater.* 138 (2017) 140–149, <https://doi.org/10.1016/j.actamat.2017.07.045>.
- [27] T.M. Mower, M.J. Long, Mechanical behavior of additive manufactured, powder-bed laser-fused materials, *Mater. Sci. Eng.* 651 (2016) 198–213, <https://doi.org/10.1016/j.msea.2015.10.068>.
- [28] T. Voisin, J.-B. Forien, A. Perron, S. Aubry, N. Bertin, A. Samanta, A. Baker, Y. Morris Wang, New insights on cellular structures strengthening mechanisms and thermal stability of an austenitic stainless steel fabricated by laser powder-bed-fusion, *Acta Mater.* 203 (2021) 116476, <https://doi.org/10.1016/j.actamat.2020.11.018>.
- [29] O. Andreau, I. Koutiri, P. Peyre, J.-D. Penot, N. Saintier, E. Pessard, T. De Terris, C. Dupuy, T. Baudin, Texture control of 316L parts by modulation of the melt pool morphology in selective laser melting, *J. Mater. Process. Technol.* 264 (2019) 21–31, <https://doi.org/10.1016/j.jmatprotec.2018.08.049>.
- [30] D. Yang, Y. Zhao, X. Kan, X. Chu, H. Sun, Z. Zhao, J. Sun, H. Wang, Twinning behavior in deformation of SLM 316L stainless steel, *Mater. Res. Express* 9 (9) (2022) 096502, <https://doi.org/10.1088/2053-1591/ac8bc7>.
- [31] T.S. Byun, B.E. Garrison, M.R. McAlister, X. Chen, M.N. Gussev, T.G. Lach, A. L. Coq, K. Linton, C.B. Joslin, J.K. Carver, F.A. List, R.R. Dehoff, K.A. Terrani, Mechanical behavior of additively manufactured and wrought 316L stainless steels before and after neutron irradiation, *J. Nucl. Mater.* 548 (2021) 152849, <https://doi.org/10.1016/j.jnucmat.2021.152849>.
- [32] S. Dryepont, P. Nandwana, P. Fernandez-Zelaia, F. List, Microstructure and high temperature tensile properties of 316L fabricated by laser powder-bed fusion, *Addit. Manuf.* 37 (2021) 101723, <https://doi.org/10.1016/j.addma.2020.101723>.
- [33] S. Gorsse, C. Hutchinson, M. Gouné, R. Banerjee, Additive manufacturing of metals: a brief review of the characteristic microstructures and properties of steels, Ti-6Al-4V and high-entropy alloys, *Sci. Technol. Adv. Mater.* 18 (1) (2017) 584–610, <https://doi.org/10.1080/14686996.2017.1361305>.
- [34] X. Zhu, Z. Zhu, T. Liu, W. Liao, Y. Du, H. Wei, Crack-free and high-strength AA2024 alloy obtained by additive manufacturing with controlled columnar-equiaxed-transition, *J. Mater. Sci. Technol.* 156 (2023) 183–196, <https://doi.org/10.1016/j.jmst.2023.01.012>.
- [35] Z. Liu, D. Zhao, P. Wang, M. Yan, C. Yang, Z. Chen, J. Lu, Z. Lu, Additive manufacturing of metals: microstructure evolution and multistage control, *J. Mater. Sci. Technol.* 100 (2022) 224–236, <https://doi.org/10.1016/j.jmst.2021.06.011>.
- [36] A.J. Godfrey, J. Simpson, D. Leonard, K. Sisco, R.R. Dehoff, S.S. Babu, Heterogeneity and solidification pathways in additively manufactured 316L stainless steels, *Metal. Mater. Trans. A* 53A (2022) 3321–3340, <https://doi.org/10.1007/s11661-022-06747-6>.
- [37] A. Prasad, L. Yuan, P. Lee, M. Patel, D. Qiu, M. Easton, D. St John, Towards understanding grain nucleation under Additive Manufacturing solidification conditions, *Acta Mater.* 195 (2020) 392–403, <https://doi.org/10.1016/j.actamat.2020.05.012>.